ORGANIC CHEMISTRY FRONTIERS

RESEARCH ARTICLE

View Article Online
View Journal | View Issue

Cite this: *Org. Chem. Front.*, 2022, **9**, 3730

Computational insights on the origin of enantioselectivity in reactions with diarylprolinol silyl ether catalysts *via* a radical pathway†

Ching Ching Lam and Jonathan M. Goodman *

Received 24th March 2022,
Accepted 4th May 2022

DOI: 10.1039/d2qo00354f

rsc.li/frontiers-organic

The stereoselective reaction of 1,4-dicarbonyls with diarylprolinol silyl ether catalysts was studied with force field and density functional theory calculations. A robust procedure has been developed for computational investigations of large and flexible chemical systems based on the conformation labelling system, ONIOM calculations and Python scripting. The change in enantiomeric excess due to variations in the catalyst can be explained based on conformational changes and structural deformations. In the enantioselectivity-determining radical addition step, the iminium in the most stable SR transition state (TS) takes up the conformation of the most stable ground state iminium (EE). The conjugated iminium in the SS TS adopts an EZ conformation to avoid potential structural deformations due to radical attacks from the more sterically hindered position. For systems with simpler catalysts, the iminium is EE for both, as the steric hindrance imposed by the substituent is not sufficient to cause this large structural deformation, and so the reaction shows poor enantioselectivity.

Introduction

Molecules containing the 1,4-dicarbonyl motif are valuable intermediates or starting materials in the synthesis of heterocycles.[1] Stereoselective synthesis of 1,4-dicarbonyls is challenging as this usually requires an inversion of polarity on one of the C=O bonds. An existing approach to access 1,4-dicarbonyls is Stetter reactions with thiamine catalysts *via* Breslow intermediates.[2,3] Recently, Melchiorre *et al.* have proposed photocatalytic routes to synthesise 1,4-dicarbonyl compounds with stereochemical control using 1,4-dihydropyridine (DHP) and diarylprolinol silyl ether catalysts (the 'amine catalysts' below, Scheme 1).[4] In the optimised trial, a high yield of 88% has been achieved with a reasonable enantiomeric excess (ee) of 76%.

Diarylprolinol silyl ether systems were first proposed by Jørgensen *et al.* to achieve enantioselective sulfenylation of aldehydes in 2005.[5,6] Further research efforts in the last decade have extended the application of the catalytic systems to other functionalisation reactions at positions neighbouring the carbonyl group *via* the formation of either an iminium or enamine molecule.[5] The catalysis of diarylprolinol silyl ether compounds has previously been studied with computational methodologies on functionalisation reactions with ionic pathways.[7] In 2014, Seebach *et al.*[8] performed density functional theory (DFT) calculations on various amine-catalysed reactions with ionic mechanisms and derived trends that correlate the size of the substituent with the reaction enantioselectivity.

The applications of diarylprolinol silyl ethers in radical pathways have not been widely explored. Unlike in ionic approaches, acyl radicals are highly reactive and achieving good enantioselectivity becomes more challenging *via* a radical route.[9] Following the success in 2013,[10] Melchiorre *et al.* have reported several enantioselective photochemical reactions with the use of amine catalysts, which include the 1,4-dicarbonyl synthesis with DHP.[4,11–13] However, the origin of the enantioselectivity for these reactions remains unexplored. In 2021, Duarte *et al.*[14] conducted computational studies on the selectivity of α-chiralbicyclo[1.1.1]pentane reactions. The reaction required amine-based catalysts and followed a similar photochemical radical route. Due to the nature of the functional groups attached to the carbonyl, the selectivity was mainly controlled by local non-covalent interactions (NCIs). Good experimental enantioselectivity has also been reported on reactions with substrates that are relatively inert to form strong NCIs, which includes the studies from Melchiorre *et al.*[4,15]

This report is based on the experimental outcome of the photocatalytic 1,4-dicarbonyl synthesis from Melchiorre *et al.*[4] We explain the enantioselectivity of the reactions from the perspective of conformational changes and structural deformations. We have also proposed a procedure for investigating

Yusuf Hamied Department of Chemistry, University of Cambridge, Lensfield Road, Cambridge, CB2 1EW, UK. E-mail: jmg11@cam.ac.uk

† Electronic supplementary information (ESI) available. See DOI: https://doi.org/10.1039/d2qo00354f

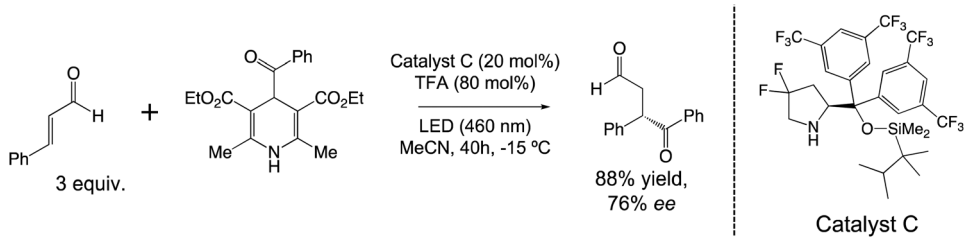

Scheme 1 The enantioselective synthesis of 1,4-dicarbonyls with a diarylprolinol silyl ether catalyst.[4]

large and structurally flexible chemical systems computationally. Automated Python pipelines have been written and applied to facilitate this effective and efficient procedure, which is potentially transferable to related chemical systems.

Computational methodologies

Conformational searching calculations were conducted in MacroModel (v11.7)[16] with Merck Molecular Force Field (MMFF).[17] DFT optimisations were performed with Gaussian 16 (Revision B.01)[18] at the B3LYP/6-31G(d) level of theory.[19–21] Single-point energy calculations were conducted at the ωB97X-D/6-311++G(d,p) level of theory.[22] Inclusion of SMD solvent models[23] in single-point energy calculations were also considered during benchmarking of the transition state (TS) $\Delta G^{\ddagger}$. 3D images of the optimised structures were generated with CYLview20,[24] PyMOL[25] and Visual Molecular Dynamics (VMD).[26]

A pipeline has been built to facilitate automations in computational investigations. The scripts were written in Python 3 using a Jupyter notebook (6.1.4).

Results and discussion

The focus of the investigation

Melchiorre *et al.* have proposed the catalytic cycle (Fig. 1) for the photocatalytic 1,4-dicarbonyl reaction.[4] Amine catalysts form conjugated iminium ions with an enal and activate the β carbon of the iminium ion for incoming attacks.[5] The DHP molecule absorbs a photon, which leads to homolytic fissions and the release of an acyl radical. The C–C bond formation between the iminium ion and the acyl radical occurs *via* a doublet pathway. The radical addition produces a cationic radical adduct as the product. The adduct needs to go through a H atom transfer (HAT) process before the iminium hydrolysis.

Based on the possibility that the iminium ion could also be excited upon absorption of a photon, we also considered an alternative mechanism (mechanism 2, electronic ESI Fig. 1B†).[27,28] The higher energy barriers of this mechanism make it less favourable than mechanism 1 in Fig. 1.†

The C–C bond formation step for each mechanism was considered computationally. The activation energy for the radical addition process ($\Delta G^{\ddagger}$ = 10.7 kcal mol^{-1}) is much lower than

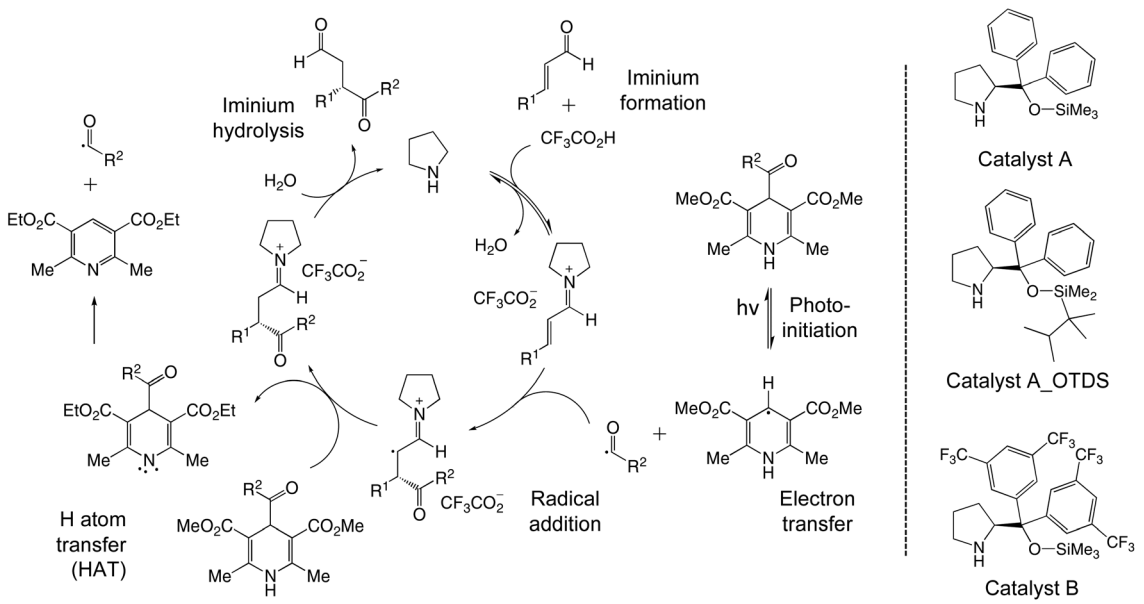

Fig. 1 The catalytic cycle proposed by Melchiorre *et al.*[4] and catalysts of interest in this study. The stereo-determining radical addition step has been highlighted in orange.

the radical coupling process ($\Delta G^{\ddagger}$ = 20.6 kcal mol^{-1}), which suggests that the reaction proceeds *via* radical attack to the ground state iminium. A simplified system has been used for the mechanistic study. The sequential step, *i.e.* the hydrogen atom transfer (HAT), was investigated and the process is feasible. For more details, see 'ESI 3.† Mechanistic studies'. Overall, the enantioselectivity determining step, which is the focus of this computational study, is the radical addition between the iminium ion and the acyl (COR^2) radical. Various systems have been studied thoroughly by considering catalysts (*i.e.* Catalyst A, A_OTDS, B and C; Fig. 1 and Scheme 1) and substrates (*i.e.* R^1 = Ph or Me and R^2 = Ph or Me) of different size and complexity.

Automations and conformation analyses

Traditionally, to obtain TS structures of complex systems, computational chemists need to follow a process of conformational searches, DFT optimisations to minima on the potential energy surface, bond freezing optimisations and TS optimisations.[29] In the case of catalyst C, the conformational searching calculations of its iminium produce 2228 conformers. Considering the size of the system (*e.g.* 86 atoms and 388 electrons in the catalyst C iminium), it is computationally costly to reoptimise and obtain a TS for all the conformers at the DFT level from the output of conformational searches. Hence, we established an efficient procedure for studying the radical addition process computationally (Fig. 2).

Firstly, we have introduced filters in the procedure, which aim to select conformers for further analyses. Filters were built on top of a conformational labelling system. The conformational labelling system was developed for classifying and labelling conformers according to their structural features. The procedure starts with the identification of the key structural features within the molecule. Fig. 3 summarises the derivations of structural feature labels. At the beginning of our investigation, only the iminium and rotamer features were included in the conformation label (Fig. 3A and B). These two structural features are known to be correlated with the energy of the system.[8,30] After the first batch of calculations, we found that a conformation label with two features is insufficient and conformers with the same conformation label can have a $\Delta\Delta G$ up to 6 kcal mol^{-1}. By inspecting the difference in structure between conformers with the same conformation label, we picked out other important structural features and introduced them into the conformation labelling system. With the current system, $\Delta\Delta G$ values of conformers with the same conformation label should be under 1.0 kcal mol^{-1}.

The key structural features and the associated labels for the cationic radical adduct are as follows: iminium (E/Z; Fig. 3A), rotamer (*syn_exo*/*syn_endo*/app; Fig. 3B), ring conformation

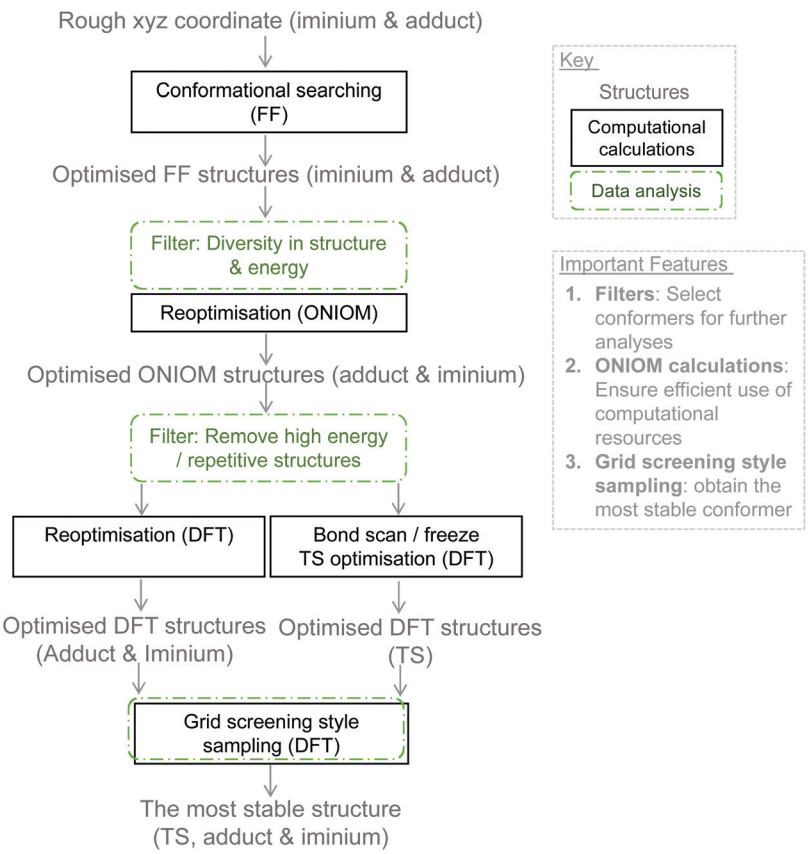

Fig. 2 An efficient computational procedure for uncovering large and flexible chemical systems. The grid screening style sampling requires both computational calculations and data analyses.

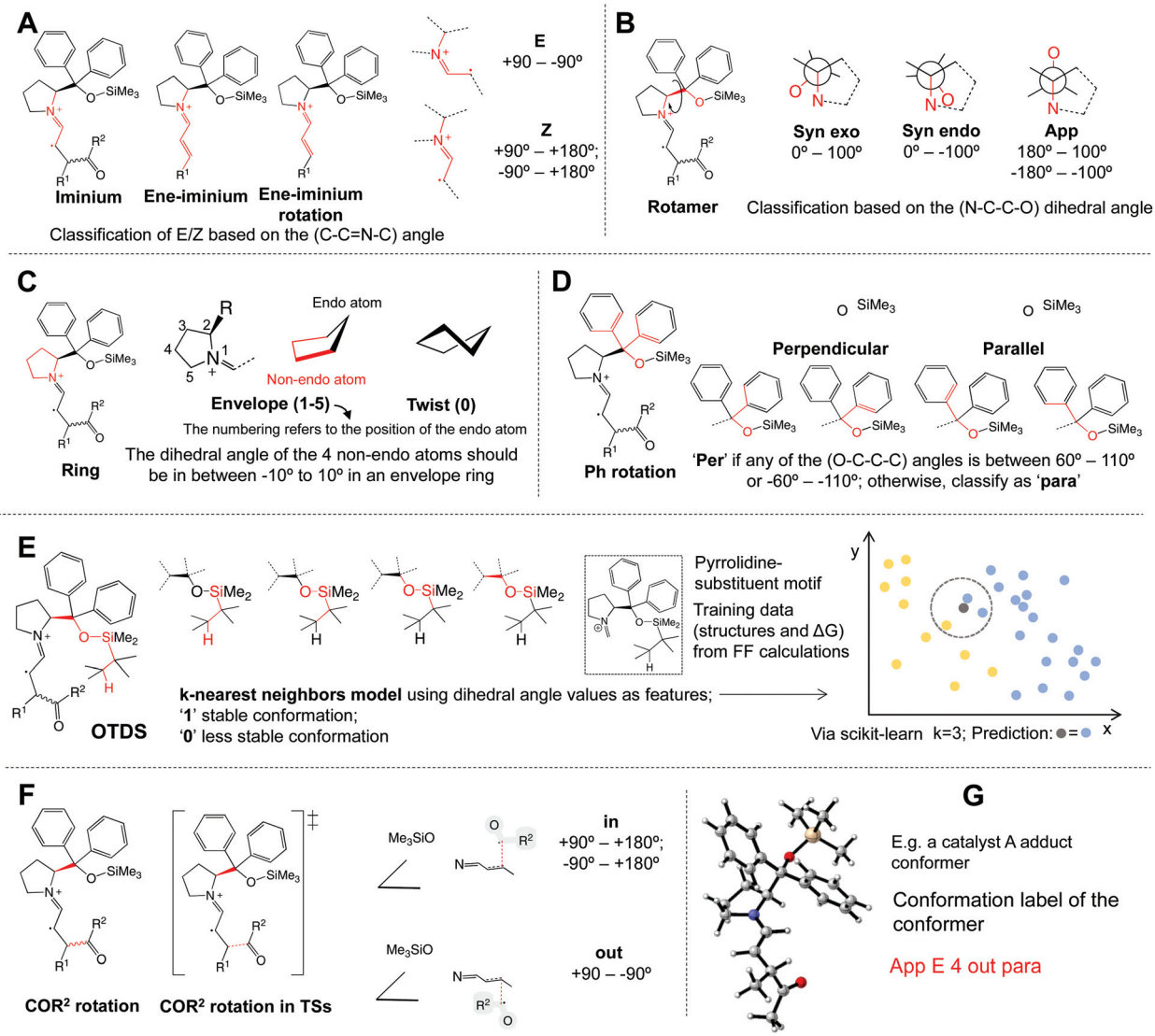

Fig. 3 The conformational labelling system: The structural feature labels are identified based on dihedral angle values. The key dihedral angles are coloured in red. A: iminium, ene-iminium and its rotation; B: ring; C: rotamer (*i.e.* the rotation of the large bulky substituent); D: Ph rotation; E: –OTDS based on k-nearest neighbours model; and F: COR^2 rotation; G. The conformation label is derived by joining the structural feature labels identified.

(envelope (1–5)/ring (0); Fig. 3C), Ph rotation (*para*/per; Fig. 3D) and COR^2 rotation (in/out; Fig. 3F). The rotamer, ring conformation and Ph rotation classifications are also applied to iminium structures. The differences between the adduct and the iminium are taken into account by the ene-iminium ion (EE/EZ/ZE/ZZ) and its rotation (*trans*-/*cis*-ene-iminium) structural feature (Fig. 3A). All the structural features for the iminium and the COR^2 rotation label are also applicable to the TS structures.

The label identification process is based on measurements of dihedral angles. For example, the iminium (E/Z) structural feature classification is based on the value of the C–C═N–C dihedral angle (Fig. 3A). A conformer with an '*E*' iminium has a $\theta_{dihedral}$(C–C═N–C) value between +90° and −90°. Conformers with a $\theta_{dihedral}$(C–C═N–C) value outside the range of +90° – −90° are regarded as '*Z*' iminiums. None of the conformers have a dihedral angle similar to the cutoff. The label identification for other structural features follows a similar logic of categorical classification based on one or multiple dihedral angle values (ESI 4.† Structural feature labels). Structures with catalyst A_OTDS and C have an –OTDS chain. With the dihedral angle values on the backbone of the –OTDS chain as features, we trained a k-nearest neighbours model based on force field (FF) data to label the stable –OTDS orientations (Fig. 3E). The stable orientations are given a label of '1' rather than '0'. The conformation label is derived by joining the structural feature labels identified (Fig. 3G).

The automated filter pipeline generates the conformation label with the xyz file of the conformers and dihedral angles of interest as the input. Based on the conformation label and the number of conformers under the same classification, conformers are selected for further analyses, *i.e.* optimisations at a

higher level of theory or TS optimisations. The filter on conformers from conformational searches aims to sample representative structures that are diverse in structure and energy. Taking catalyst C iminium as an example, 63 representatives are selected from 2228 MMFF structures for reoptimising at a high level of theory. The sample of 63 conformers includes both the frequently appeared structures and outliers that are different from other structures in the output file. The filter on the reoptimised conformers, which are applied after the initial screening step, focuses on removing repetitive and high energy structures (see ESI 5.† Filters).

In the initial screening step, ONIOM optimisations[31] were performed on structures from conformational searches at the ONIOM(B3LYP/6-31G(d):UFF) level of theory, *i.e.* part of the system is optimised at the cheaper UFF (universal force field) level.[32] We found no significant difference between ΔG from ONIOM calculations and ΔG at the DFT level if the border of the two layers were carefully chosen (ESI Fig. 7†). On average, based on the calculations on SR adducts with catalyst C and B, the computational time for ONIOM calculations is only 1/3 of DFT level calculations typically. Thus, initial sampling with ONIOM calculations allows a large number of conformers to be screened and studied at a relatively low computational cost.

Finally, grid screening style samplings were conducted to ensure that the most stable structure was considered and obtained. Here, the data from conformation labelling system was used as a guide for further conformation sampling. The process began with exploring correlations between structural features and ΔG of the system with statistical analyses through box plots (ESI Fig. 8†). The box plot analyses allowed generalisations to be made. For example, conformers of the catalyst B TS with the '*syn_exo*' and 'per' labels are noticeably more stable than conformers with 'app', '*syn_endo*' and '*para*' labels. Sometimes, more than one structural feature label may contribute to a stable conformation. In the case of catalyst B TSs, '3' *vs.* '4' (ring conformation), 'EE' *vs.* 'EZ' (ene-iminium) and 'in' *vs.* 'out' (COR rotation) are competing structural features. Additional structures with different combinations of these labels were sampled in a grid screening style if they were not already presented in the data set of optimised structures (ESI Fig. 9†).

The improved procedure allows efficient use of computational resources and is effective in obtaining the key structures for analyses. This procedure was developed during the investigation on reactions with catalyst A and A_OTDS and has been successfully applied on the more complex systems with catalyst B and C.

Origin of the enantioselectivity

The computational $\Delta G^{\ddagger}$ and the conformation label of the most stable conformations for selective systems are presented in Tables 1 and 2 (see Tables 8 and 9† for the complete result tables). The trend in $\Delta\Delta G^{\ddagger}$ generally agrees with the experimental results. In addition to the data from Melchiorre *et al.*, we also compared our results with the work from Yu *et al.*[33] Yu *et al.* have also reported a highly similar radical route for synthesising 1,4-dicarbonyls. Their reactions also involved amine catalysts but used Ru(I) complex for photoinitiations and generations of COR^2 radical. Pathways *via* a SR TS lead to the major product. In Table 1, as the steric demand of the catalyst increases, SR pathways become more kinetically favourable than SS pathways. Changing R^1 from –Me to –Ph group also contributes to a higher $\Delta\Delta G^{\ddagger}$. It is important to highlight that $\Delta G^{\ddagger}$ values of SR pathways remain almost unchanged regardless of the changes in the steric bulkiness and electronic properties of the catalyst. This suggests that the radical addition step is not the yield-determining step. We suspect that the HAT process might be yield-limiting. For more details, please see 'ESI 3.† Mechanistic studies'.

A benchmarking study has been conducted on the keys TS structures. Firstly, we want to highlight the importance of including a solvent model in single point calculations, which improves the accuracy of the TS $\Delta G^{\ddagger}$. $\Delta\Delta G^{\ddagger}$ values show a closer match to the experimental result. Secondly, there are often several TS conformers with very similar $\Delta G^{\ddagger}$ values to the most stable TS, especially for the SS TSs. Hence, the most

Table 1 The calculated kinetic data (level of theory: ωB97X-D/6-311++G(d,p)/SMD/CH_3CN//B3LYP/6-31G(d); unit: kcal mol^{-1}) and experimental percentage enantiomeric excess (%ee) from the work of Melchiorre *et al.*[4] and Yu *et al.*[33]

	R^1 = Me; R^2 = Ph			R^1 = Ph; R^2 = Ph		
	$\Delta G^{\ddagger}$	$\Delta\Delta G^{\ddagger}$	Exp. %ee	$\Delta G^{\ddagger}$	$\Delta\Delta G^{\ddagger}$	Exp. %ee
Catalyst A						
SR	12.2	0.5	—	—	—	12[b]
SS	11.7	0.0		—	—	
Catalyst A_OTDS						
SR	11.6	0.0	—	—	—	—
SS	12.0	0.4		—	—	
Catalyst B						
SR	11.8	0.3	—	12.4	0.0	27[a]/38[b]
SS	11.5	0.0		14.7	2.3	
Catalyst C						
SR	11.6	0.0	69[a]	11.2	0.0	76[a]/80[b]
SS	13.6	2.0		13.7	2.5	

[a] From Melchiorre *et al.*[4] [b] From Yu *et al.*[33]

Table 2 The conformation label of the iminium in the most stable TS conformer and the conformation label of the most stable ground state iminium conformer at the ωB97X-D/6-311++G(d,p)/SMD/CH_3CN//B3LYP/6-31G(d) level of theory. All the structures presented below have a '*trans*-ene-iminium' label

Catalyst	SR TS	SS TS	Iminium
R^1 = Me; R^2 = Ph			
A	*syn_exo* EE 3 per	*syn_exo* EE 3 per	*syn_exo* EE 3 per
A_OTDS	*syn_exo* EE 3 per 1	*syn_exo* EE 3 per 0	*syn_exo* EE 3 per 1
B	*syn_exo* EE 3 per	*syn_exo* EZ 3 per	*syn_exo* EE 3 per
C	*syn_exo* EE 4 per 1	*syn_exo* EE 4 per 1	*syn_exo* E 0 per 1
R^1 = Ph; R^2 = Ph			
B	*syn_exo* EE 3 per	*syn_exo* EZ 3 per	*syn_exo* EE 3 per
C	*syn_exo* EE 0 per 1	*syn_exo* EZ 5 per 1	*syn_exo* EE 0 per 1

stable SS TS conformer obtained with different DFT functionals may have subtle structural differences. Nevertheless, the overall trend stated in the previous paragraph remains consistent (ESI 9.† Benchmarking).

Intrinsic reaction coordinate (IRC) or quick reaction coordinate (QRC)[34] calculations are performed to check that the TS is on the reaction path of interest. We have conducted further analyses taking into consideration of all the optimised TS conformers (Fig. 5) by plotting $\Delta\Delta G^{\ddagger}$ of the TSs against ΔG of the iminium taken from the IRC or QRC of the corresponding TS (Fig. 4). For catalyst A, a strong linear trend (Pearson's $r = 0.94$) in the plot between the two variables shows that the stability of the iminium ion is strongly correlated to the activation energy of the process. Increasing the complexity and steric demand of the catalyst leads to a drop in the Pearson's r value of the plot. The gradient and y-intercept of the line of best fit also deviate from 1.0 and 0.0. The trend implies that the iminium in TSs with a low $\Delta\Delta G^{\ddagger}$ may take up a less stable conformation as the steric hindrance increases.

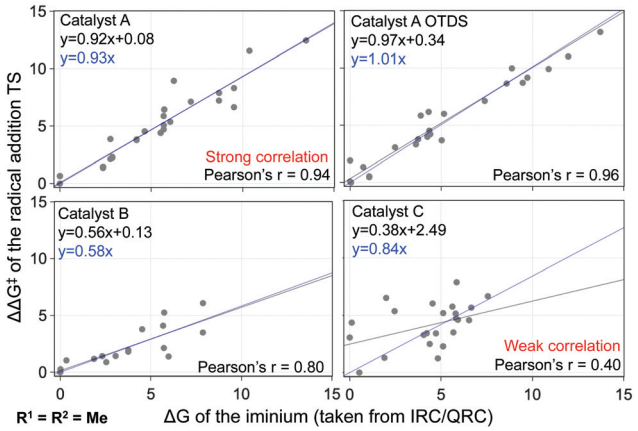

Fig. 4 $\Delta\Delta G^{\ddagger}$ values of the TSs *vs.* ΔG of the iminium taken from the IRC or QRC[34] plots for the radical addition process in reactions with catalyst A, A_OTDS, B and C. The substituents on the enal and COR^2 radical, R^1 and R^2, are both Me group (Fig. 1). The calculations were performed at the ωB97X-D/6-311G(d,p)//B3LYP/6-31G(d) level of theory. (unit: kcal mol^{-1}).

Looking at the most stable TS structures, the iminium ion in SR TSs always has the same conformation label (EE) as the most stable ground state iminium (Table 2). In the radical addition process for the SR adducts, the COR^2 radical can simply attack with the 'in' orientation without interfering with the bulky substituent in the iminium. However, this does not apply to the SS TSs. The iminium ions in the most stable SS TSs often need to adopt a less stable EZ conformation, unlike the group state iminium. The difference in iminium conformation may be due to local interactions or structural deformations during the reaction process.

Local interactions refer to either favourable non-covalent interactions (NCIs) or unfavourable steric clashes. We conducted NCI plot analyses on the TSs.[35] Various TS conformers, including the less stable conformers, for processes with different catalysts have been studied and consistent results have been obtained. The NCIs between the COR^2 radical and

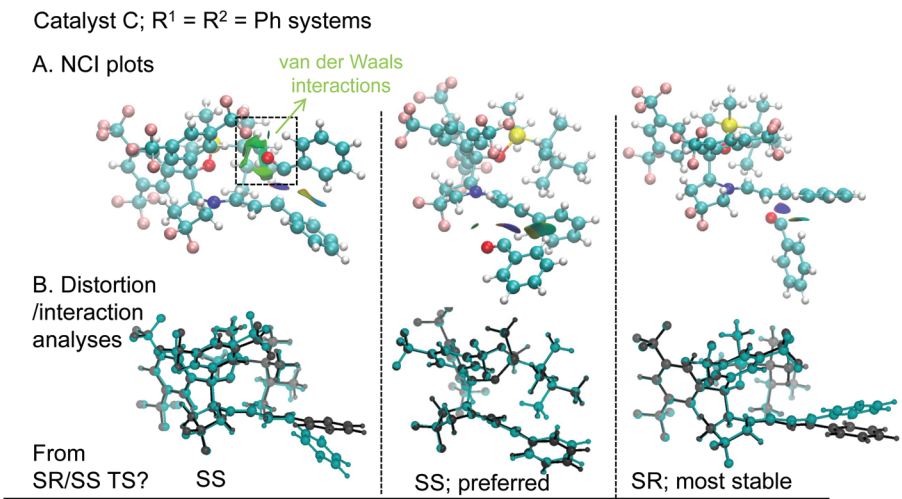

	syn_exo EE 4 in per 1	syn_exo EZ 5 out per 1	syn_exo EE 0 out per 1
Relative energy	12.8	2.8	3.4
TS $\Delta\Delta G^{\ddagger}$	5.7	2.5	0.0
Iminium ΔG	0.0	3.3	0.0

Key: TS structure; ground state iminium from QRC

Fig. 5 Analyses to examine the origin of enantioselectivity: the diagram above is based on catalyst C TSs. A. Non-covalent interaction (NCI) plot analyses: the colour of the surfaces within the TS structures indicates the nature of the interactions (*i.e.* blue = attractive, red = repulsive and green = weak van der Waals interactions); B: Distortion-interaction analyses for the iminium structure from TSs of the radical addition process. Structural alignment diagrams between the iminium structure at the TS and the ground state iminium are also given. The conformation label of the TSs is included in the table. All the TSs presented have a '*trans*-ene-iminium' label (unit: kcal mol^{-1}).

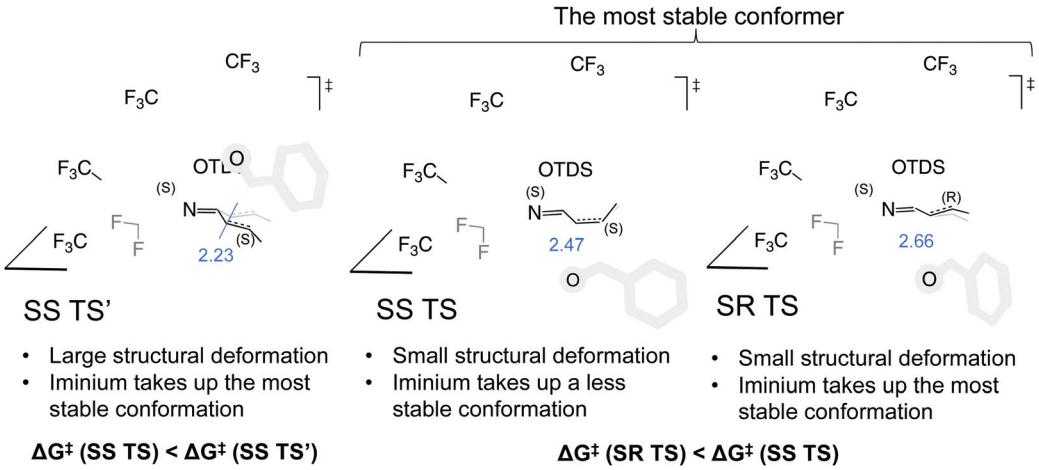

Fig. 6 The origin of enantioselectivity: catalyst C TSs (R^1 = Ph; R^2 = Ph) are used as examples. The iminium in the SR TS takes up the most stable conformation with little structural deformations. In SS TS, small structural deformations within the iminium are at the cost of changing the conformation. Thus, $\Delta G^{\ddagger}$ (SR TS) < $\Delta G^{\ddagger}$ (SS TS). In SS TS', the iminium takes up the most stable conformation, which leads to large structural deformations. Hence, $\Delta G^{\ddagger}$ (SS TS) < $\Delta G^{\ddagger}$ (SS TS'). The bond length values of the forming C–C bonds in Å are labelled in blue. The SS and SR TS lead to the SS and SR adduct respectively.

the iminium ion are mainly weak van der Waals interactions. In Fig. 5A, examples of NCI plot structures are given. The van der Waals interactions are indicated by green surfaces within the structures. Local interactions do not play a significant role in determining the orientation of the iminium in the most stable SS TS regardless of the size of the substituent on the catalyst.

The overall structural deformation, as opposed to specific rotational conformational changes, is considered with distortion/interaction analyses.[36] The relative energy, which measures the extent of distortion between the iminium structure from the TS relative to the ground state iminium from QRC in terms of energy, was calculated (Fig. 5B – take catalyst C radical addition TSs as examples). Relative energy values correlate positively with $\Delta\Delta G^{\ddagger}$ of the corresponding TS (see plots of relative energy *vs.* $\Delta\Delta G^{\ddagger}$ in ESI Fig. 14†). In catalyst C systems, the relative energy is much higher when the iminium in the SS TS takes up the same conformation label, EE, as the most stable ground state iminium. The difference in the extend of deformation is also reflected in alignment diagrams in Fig. 5B. The iminium in the preferred SS TS takes up a less stable EZ conformation to minimise the overall deformational distortion. The change in the iminium conformation is at the cost of raising the kinetic barrier of the radical addition process, which leads to the stereo outcome of the reaction. For simple systems with a less sterically bulk catalyst (*e.g.* catalyst A system; R^1 = R^2 = Me; low experimental %ee), the most stable SS and SR TS have the same conformation label. Here, the energy cost of distorting the structure is presumably lower than the cost of changing the iminium conformation. For catalyst A (R^1 = Me; R^2 = Me), the corresponding relative energy for the most stable SS and SR TS differs by only 1.0 kcal mol^{-1}.

Changing from –OTMS to –OTDS always led to a noticeable increase in %ee and $\Delta\Delta G^{\ddagger}$, regardless of the complexity of the system (*i.e.* from catalyst A to A_OTDS or from catalyst B to C systems) (Table 1). Introducing the $-CF_3$ groups only (*i.e.* moving from catalyst A to B systems) gave similar %ee and $\Delta\Delta G^{\ddagger}$ values. However, having both the –OTDS chain and $-CF_3$ groups in the catalyst (*i.e.* moving from catalyst A_OTDS to C systems) produced the best enantioselectivity outcome. The most stable TSs take up a *syn_exo* orientation, where the $-CF_3$ substituted phenyl groups are on average further away from the site of radical addition compared to the –OTDS chain. Thus, $-CF_3$ groups indirectly influence the reaction site by reducing the steric flexibility of the –OTDS chain. The enhanced structural restrictions force iminium ions on taking up a less stable structure at the TSs. The electronic impact of introducing the $-CF_3$ groups is insignificant. Hirshfeld charge analyses show that the charge distribution at the site of radical additions (*i.e.* the N=C–C=C region) does not vary extensively between iminium ions with different catalysts (ESI Fig. 16†).

In addition to the work from Melchiorre *et al.*[4] and Yu *et al.*,[33] we have also considered the experimental results from other amine-catalysed reactions *via* a radical pathway.[10–14,37] The above model and lesson learnt can also be applied to similar reactions given that the substrates (*i.e.* attacking radical and enal, ketone or aldehyde) are generally inert to form strong non-covalent interactions.

Conclusions

In conclusion, we have proposed and assembled an effective procedure for computational investigations on the reaction of interests in this study. Automations and Python pipelines have been implemented and the script can be found on GitHub (**https://github.com/Goodman-lab/Script_im**). The ideas behind the procedure are also transferrable and can be applied to other large, structurally complex and highly flexible

organic systems. We will continue improving the robustness of the process in future studies.

The photochemical synthesis of 1,4-dicarbonyl compounds with amine catalysts has been studied computationally with DFT and FF calculations. Focusing on the radical addition step between the iminium and the COR^2 radical, origin of enantioselectivity becomes clear. The direction of attack of the COR^2 radical and its interactions with the bulky substituent on the catalyst is not sufficient to explain the difference in $\Delta G^{\ddagger}$ value. The conformation labelling system and distortion/interaction analyses highlight that the iminium in the preferred SS TS adopts a less stable EZ conformation to reduce the overall structural deformation. The enantioselective outcome of the reaction is due to the conformation difference between the iminium in the SR and SS TS, which contributes to the $\Delta\Delta G^{\ddagger}$ value significantly. For systems with reduced substituent size in the catalyst, the iminium adopts the same structure in SS and SR TSs (Fig. 6). The small structural deformation difference between the iminium in the TSs leads to the insignificant $\Delta\Delta G^{\ddagger}$ values and poor enantioselectivity experimentally.

Data availability

Data for this paper is available: **https://doi.org/10.17863/CAM.84437**.

Conflicts of interest

There are no conflicts of interest.

Acknowledgements

We thank Trinity College Cambridge and Krishnan-Ang Studentships Programme for the financial support of this project. This work was performed using resources provided by the Cambridge Service for Data Driven Discovery (CSD3), operated by the University of Cambridge Research Computing Service (**https://www.csd3.cam.ac.uk**), provided by Dell EMC and Intel using Tier-2 funding from the Engineering and Physical Sciences Research Council (capital grant EP/P020259/1) and DiRAC funding from the Science and Technology Facilities Council (**https://www.dirac.ac.uk**).

Notes and references

1 G. Piancatelli, M. D'Auria and F. D'OnoFrio, Synthesis of 1,4-Dicarbonyl Compounds and Cyclopentenones from Furans, *Synthesis*, 1994, 867–889.
2 R. C. Gomes, R. C. Barcelos, M. T. Rodrigues, H. Santos and F. Coelho, Intermolecular Stetter Reactions on Morita-Baylis-Hillman Adducts: an Approach to Highly Functionalized 1,4-Dicarbonyl Compounds, *ChemistrySelect*, 2017, **2**, 926–930.
3 H. Stetter, Catalyzed Addition of Aldehydes to Activated Double Bonds—A New Synthetic Approach, *Angew. Chem., Int. Ed. Engl.*, 1976, **15**, 639–647.
4 G. Goti, B. Bieszczad, A. Vega-Peñaloza and P. Melchiorre, Stereocontrolled Synthesis of 1,4-Dicarbonyl Compounds by Photochemical Organocatalytic Acyl Radical Addition to Enals, *Angew. Chem., Int. Ed.*, 2019, **58**, 1213–1217.
5 K. L. Jensen, G. Dickmeiss, H. Jiang, Ł. U. Albrecht and K. A. Jørgensen, The Diarylprolinol Silyl Ether System: A General Organocatalyst, *Acc. Chem. Res.*, 2012, **45**, 248–264.
6 M. Marigo, T. C. Wabnitz, D. Fielenbach and K. A. Jørgensen, Enantioselective organocatalyzed α sulfenylation of aldehydes, *Angew. Chem., Int. Ed.*, 2005, **44**, 794–797.
7 K. S. Halskov, B. S. Donslund, B. M. Paz and K. A. Jørgensen, Computational Approach to Diarylprolinol-Silyl Ethers in Aminocatalysis, *Acc. Chem. Res.*, 2016, **49**, 974–986.
8 Y. Hayashi, D. Okamura, T. Yamazaki, Y. Ameda, H. Gotoh, S. Tsuzuki, T. Uchimaru and D. Seebach, A theoretical and experimental study of the effects of silyl substituents in enantioselective reactions catalyzed by diphenylprolinol silyl ether, *Chem. – Eur. J.*, 2014, **20**, 17077–17088.
9 S.-H. Xiang and B. Tan, Advances in asymmetric organocatalysis over the last 10 years, *Nat. Commun.*, 2020, **11**, 3786.
10 E. Arceo, I. D. Jurberg, A. Álvarez-Fernández and P. Melchiorre, Photochemical activity of a key donor-acceptor complex can drive stereoselective catalytic α-alkylation of aldehydes, *Nat. Chem.*, 2013, **5**, 750–756.
11 M. Silvi, C. Verrier, Y. P. Rey, L. Buzzetti and P. Melchiorre, Visible-light excitation of iminium ions enables the enantioselective catalytic β-alkylation of enals, *Nat. Chem.*, 2017, **9**, 868–873.
12 E. Le Saux, D. Ma, P. Bonilla, C. M. Holden, D. Lustosa and P. Melchiorre, A General Organocatalytic System for Enantioselective Radical Conjugate Additions to Enals, *Angew. Chem., Int. Ed.*, 2021, **60**, 5357–5362.
13 M. Silvi, E. Arceo, I. D. Jurberg, C. Cassani and P. Melchiorre, Enantioselective organocatalytic alkylation of aldehydes and enals driven by the direct photoexcitation of enamines, *J. Am. Chem. Soc.*, 2015, **137**, 6120–6123.
14 M. L. J. Wong, A. J. Sterling, J. J. Mousseau, F. Duarte and E. A. Anderson, Direct catalytic asymmetric synthesis of α-chiral bicyclo[1.1.1]pentanes, *Nat. Commun.*, 2021, **12**, 1644.
15 A. Vega-Peñaloza, S. Paria, M. Bonchio, L. Dell'Amico and X. Companyó, Profiling the privileges of pyrrolidine-based catalysts in asymmetric synthesis: From polar to light-driven radical chemistry, *ACS Catal.*, 2019, **9**, 6058–6072.
16 *Schrödinger Release 2021-2: Maestro*, Schrödinger LLC, New York NY, 2021.
17 T. A. Halgren, Merck molecular force field. I. Basis, form, scope, parameterization, and performance of MMFF94, *J. Comput. Chem.*, 1996, **17**, 490–519.
18 M. J. Frisch, G. W. Trucks, H. B. Schlegel, G. E. Scuseria, M. A. Robb, J. R. Cheeseman, G. Scalmani, V. Barone,

G. A. Petersson, H. Nakatsuji, X. Li, M. Caricato, A. V. Marenich, J. Bloino, B. G. Janesko, R. Gomperts, B. Mennucci, H. P. Hratchian, J. V. Ortiz, A. F. Izmaylov, J. L. Sonnenberg, D. Williams-Young, F. Ding, F. Lipparini, F. Egidi, J. Goings, B. Peng, A. Petrone, T. Henderson, D. Ranasinghe, V. G. Zakrzewski, J. Gao, N. Rega, G. Zheng, W. Liang, M. Hada, M. Ehara, K. Toyota, R. Fukuda, J. Hasegawa, M. Ishida, T. Nakajima, Y. Honda, O. Kitao, H. Nakai, T. Vreven, K. Throssell, J. A. Montgomery Jr., J. E. Peralta, F. Ogliaro, M. J. Bearpark, J. J. Heyd, E. N. Brothers, K. N. Kudin, V. N. Staroverov, T. A. Keith, R. Kobayashi, J. Normand, K. Raghavachari, A. P. Rendell, J. C. Burant, S. S. Iyengar, J. Tomasi, M. Cossi, J. M. Millam, M. Klene, C. Adamo, R. Cammi, J. W. Ochterski, R. L. Martin, K. Morokuma, O. Farkas, J. B. Foresman and D. J. Fox, *Gaussian 16 (Revision B.01)*, Gaussian, Inc., Wallingford CT, 2016.

19 A. D. Becke, Density-functional exchange-energy approximation with correct asymptotic behavior, *Phys. Rev. A*, 1988, **38**, 3098–3100.

20 C. Lee, W. Yang and R. G. Parr, Development of the Colle-Salvetti correlation-energy formula into a functional of the electron density, *Phys. Rev. B: Condens. Matter Mater. Phys.*, 1988, **37**, 785–789.

21 A. D. Becke, Density-functional thermochemistry. III. The role of exact exchange, *J. Chem. Phys.*, 1993, **98**, 5648–5652.

22 J.-D. Chai and M. Head-Gordon, Long-range corrected hybrid density functionals with damped atom–atom dispersion corrections, *Phys. Chem. Chem. Phys.*, 2008, **10**, 6615–6620.

23 A. V. Marenich, C. J. Cramer and D. G. Truhlar, Universal Solvation Model Based on Solute Electron Density and on a Continuum Model of the Solvent Defined by the Bulk Dielectric Constant and Atomic Surface Tensions, *J. Phys. Chem. B*, 2009, **113**, 6378–6396.

24 CYLview20, Université de Sherbrooke, 2020 **https://www.cylview.org** (accessed November 02, 2020).

25 *The PyMOL Molecular Graphics System (Version 2.0)*, Schrödinger LLC., New York, NY, 2015.

26 W. Humphrey, A. Dalke and K. Schulten, VMD: Visual molecular dynamics, *J. Mol. Graphics*, 1996, **14**, 33–38.

27 P. Bonilla, Y. P. Rey, C. M. Holden and P. Melchiorre, Photo-Organocatalytic Enantioselective Radical Cascade Reactions of Unactivated Olefins, *Angew. Chem., Int. Ed.*, 2018, **57**, 12819–12823.

28 G. B. Shen, L. Xie, H. Y. Yu, J. Liu, Y. H. Fu and M. Yan, Theoretical investigation on the nature of 4-substituted Hantzsch esters as alkylation agents, *RSC Adv.*, 2020, **10**, 31425–31434.

29 Y. H. Lam, M. N. Grayson, M. C. Holland, A. Simon and K. N. Houk, Theory and Modeling of Asymmetric Catalytic Reactions, *Acc. Chem. Res.*, 2016, **49**, 750–762.

30 A. Claraz, G. Sahoo, D. Berta, Á. Madarász, I. Pápai and P. M. Pihko, A Catalyst Designed for the Enantioselective Construction of Methyl- and Alkyl-Substituted Tertiary Stereocenters, *Angew. Chem., Int. Ed.*, 2016, **55**, 669–673.

31 L. W. Chung, W. M. C. Sameera, R. Ramozzi, A. J. Page, M. Hatanaka, G. P. Petrova, T. V. Harris, X. Li, Z. Ke, F. Liu, H. B. Li, L. Ding and K. Morokuma, The ONIOM Method and Its Applications, *Chem. Rev.*, 2015, **115**, 5678–5796.

32 A. K. Rappe, C. J. Casewit, K. S. Colwell, W. A. Goddard and W. M. Skiff, UFF, a full periodic table force field for molecular mechanics and molecular dynamics simulations, *J. Am. Chem. Soc.*, 1992, **114**, 10024–10035.

33 J. J. Zhao, H. H. Zhang, X. Shen and S. Yu, Enantioselective Radical Hydroacylation of Enals with α-Ketoacids Enabled by Photoredox/Amine Cocatalysis, *Org. Lett.*, 2019, **21**, 913–916.

34 J. M. Goodman and M. A. Silva, QRC: a rapid method for connecting transition structures to reactants in the computational analysis of organic reactivity, *Tetrahedron Lett.*, 2003, **44**, 8233–8236.

35 J. Contreras-García, E. R. Johnson, S. Keinan, R. Chaudret, J. P. Piquemal, D. N. Beratan and W. Yang, NCIPLOT: A program for plotting noncovalent interaction regions, *J. Chem. Theory Comput.*, 2011, **7**, 625–632.

36 A. G. Green, P. Liu, C. A. Merlic and K. N. Houk, Distortion/Interaction Analysis Reveals the Origins of Selectivities in Iridium-Catalyzed C–H Borylation of Substituted Arenes and 5-Membered Heterocycles, *J. Am. Chem. Soc.*, 2014, **136**, 4575–4583.

37 E. Larionov, M. M. Mastandrea and M. A. Pericas, Asymmetric visible-light photoredox cross-dehydrogenative coupling of aldehydes with xanthenes, *ACS Catal.*, 2017, **7**, 7008–7013.

